



Viscoinertial regime of immersed granular flows

L. Amarsid,^{1,2,3,*} J.-Y. Delenne,^{4,†} P. Mutabaruka,^{5,‡} Y. Monerie,^{2,3,§} F. Perales,^{1,6,||} and F. Radjai^{2,3,5,¶}

¹IRSN, PSN, CE Cadarache, BP3-13115 St Paul-Lez-Durance Cedex, France

²LMGC, CNRS, University of Montpellier, 163 rue Auguste Broussonnet, 34090 Montpellier, France

³Laboratoire MIST, IRSN-CNRS, University of Montpellier, France

⁴IATE, UMR1208 INRA-CIRAD, University of Montpellier–SupAgro, 34060 Montpellier, France

⁵<MSE>², UMI CNRS-MIT, Massachusetts Institute of Technology, 77 Massachusetts Avenue, Cambridge, Massachusetts 02139, USA

⁶Laboratoire MIST, IRSN-CNRS, University of Montpellier 2, France

(Received 13 February 2017; published 5 July 2017)

By means of extensive coupled molecular dynamics–lattice Boltzmann simulations, accounting for grain dynamics and subparticle resolution of the fluid phase, we analyze steady inertial granular flows sheared by a viscous fluid. We show that, for a broad range of system parameters (shear rate, confining stress, fluid viscosity, and relative fluid-grain density), the frictional strength and packing fraction can be described by a modified inertial number incorporating the fluid effect. In a dual viscous description, the effective viscosity diverges as the inverse square of the difference between the packing fraction and its jamming value, as observed in experiments. We also find that the fabric and force anisotropies extracted from the contact network are well described by the modified inertial number, thus providing clear evidence for the role of these key structural parameters in dense suspensions.

DOI: 10.1103/PhysRevE.96.012901

I. INTRODUCTION

The rheology of granular materials immersed in a viscous fluid is fundamental for modeling many natural flows and industrial applications [1–3]. The flow can be driven by particle motions, as in submarine avalanches, or by the fluid, like in sediment transport in a river. The immersed flow of non-Brownian particles is characterized by its packing fraction Φ and bulk friction coefficient $\mu = \sigma_t/\sigma_s$, where σ_t is shear stress and σ_s is the normal stress applied on the granular phase. The fluid affects granular flow by its viscosity η_f in combination with the shear rate $\dot{\gamma}$ and σ_s via the dimensionless viscous number $I_v = \eta_f \dot{\gamma}/\sigma_s$, which represents the ratio of the Stokes time $t_{St} = \eta_f/\sigma_s$ and flow time $t_f = \dot{\gamma}^{-1}$ [4]. Hence, the rheology of an immersed granular material can be described by two functions $\mu(I_v)$ and $\Phi(I_v)$, both tending smoothly to their critical values μ_0 and Φ_0 as $I_v \rightarrow 0$.

This frictional description has its dual viscous description in which the packing fraction Φ is the control parameter, and the flow is described by effective normal and shear viscosities η_n and η_t , respectively [4], defined by $\sigma_n = \eta_n \dot{\gamma}$ and $\sigma_t = \eta_t \dot{\gamma}$, where σ_n is the *internal* normal stress of the granular packing. We note that σ_n can be different from the applied normal stress σ_s due to dynamic effects or in the presence of a suspending fluid, as we shall see below.

The functions $\eta_n(\Phi)$ and $\eta_t(\Phi)$ are classically determined from flow experiments at imposed volume, but can also be deduced from $\mu(I_v)$, $\Phi(I_v)$, and the definition of I_v by assuming $\sigma_n = \sigma_s$. This yields $\eta_n(\Phi) = \eta_f/I_v(\Phi)$ and $\eta_t(\Phi) =$

$\eta_f \mu[I_v(\Phi)]/I_v(\Phi)$. This shows that the effective viscosities diverge when $\Phi \rightarrow \Phi_0$. The only difference between pressure-imposed and volume-imposed flows is that in the latter case the particles cease to flow at the jamming packing fraction Φ_0 , whereas in the former the flow continues. This mapping between the two descriptions was used by Boyer *et al.* to get experimentally as close as possible to the jamming packing fraction Φ_0 by means of a pressure-controlled flow and to deduce the algebraic divergence of η_t and η_n as $[\Phi_0 - \Phi]^{-2}$ [4].

The issue with I_v as control parameter is that the limit values μ_0 and Φ_0 do not characterize only the material but depend on the inertial number $I = \dot{\gamma} d(\rho_s/\rho_f)^{1/2}$, where d is the mean particle diameter and ρ_s is particle density [5]. This means that, in scaling effective properties of the flow, I_v is not simply a replacement for I in the presence of a fluid, as suggested by Boyer *et al.* [4], but the effective flow properties are controlled by both I and I_v . Trulsson *et al.* partially addressed this issue by molecular dynamics (MD) simulations with a fluid drag force applied to all particle centers [6]. Their results seem to support the idea that a general control parameter combining I and I_v can account for both inertial and viscous effects in a unified framework. However, since the fluid was introduced only through its drag force effect, it is unclear whether this framework can account for other major fluid parameters such as density and volume effects, which are crucial in the dense limit, as well as for lift forces induced by shear. Indeed, the relative density $r = \rho_s/\rho_f$, where ρ_f is fluid density, controls the flow regime [7]. In the same way, the fluid volume between particles carries negative or positive dynamic pore pressures, which in the dense regime should strongly affect particle dynamics. Hence, the framework presented by Trulsson *et al.* may simply be a consequence of drag forces directly introduced at the particle level. This means that the visco-inertial flow needs to be investigated by means of fully resolved simulations of the fluid phase.

In this paper, we analyze the effective flow behavior in the visco-inertial regime using extensive MD simulations

*lhassan.amarsid@umontpellier.fr

†jean-yves.delenne@supagro.inra.fr

‡pmutabar@mit.edu

§yann.monerie@umontpellier.fr

||frederic.perales@irsn.fr

¶franck.radjai@umontpellier.fr; fradjai@mit.edu

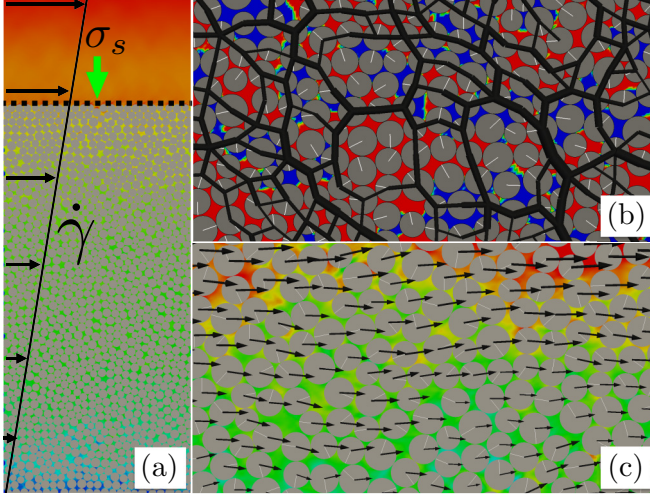


FIG. 1. (a) Schematics of the simulated system. (b) Snapshot of fluid pressure field and contact force chains. (c) Snapshot of fluid and particle velocity fields.

for particle dynamics interfaced with the lattice Boltzmann method (LBM) for the dynamics of the fluid phase [8–10]. More than 70 long-run simulations with a total processing (CPU) time of about 10^5 h cover a broad range of the values of fluid phase parameters (η_f and ρ_f), particle phase parameters (ρ_s , σ_s), and shear rate $\dot{\gamma}$. As we shall see, the effective flow properties remarkably scale with a modified inertial number that combines particle-inertial and viscous forces, provided the lift forces are taken into account. This result supports the suggestion by Trulsson *et al.* and considerably extends its scope [6]. In particular, it raises another issue as to the role of the modified inertial parameter with respect to the granular microstructure. We show that the contact and force anisotropies scale with the modified inertial number, revealing thus the origins of enhanced friction coefficient in the presence of the fluid.

II. SYSTEM DESCRIPTION AND PARAMETERS

Figure 1 displays the simulated system as well as two snapshots representing the fluid pressure field and contact force chains, on one hand, and particle-fluid velocity fields, on the other hand. The particles are disks of mean diameter $d = 2.5 \times 10^{-3}$ m and distributed in the range $[d_{\min}, d_{\max}]$ with $d_{\min} = 0.6d_{\max}$ to prevent long-range ordering of the particles. The confining stress σ_s is applied on the top wall, compressing the granular column. This wall is fully permeable to the fluid, which fills a larger domain of constant volume. Both the fluid and particles are periodic along the flow. The particles are initially distributed randomly in the box and assembled by downward motion of the top mobile wall under the action of σ_s .

The LBM was used for the simulations of the fluid phase, assumed to be an incompressible fluid governed by Navier-Stokes equations. We used the multirelaxation time (MRT) approach for the collision operator. It is computationally more costly but provides smooth hydrodynamic fields. It was interfaced with MD for the simulation of the particle phase.

In order to allow the fluid to flow between pores, we add at least one fluid node to the contact zones between each pair of particles. The node plays the same role as constrictions between pores in three dimensions (3D). The permeability of the structure is controlled by the number of fluid nodes added in contact zones. A brief description of LBM is given in Appendix A. A uniform velocity gradient $\dot{\gamma}$ is applied to the fluid nodes at domain boundary to generate a plane Couette flow. The fluid is initially at rest and the shear rate $\dot{\gamma}$ is increased gradually from zero to its final value. The above boundary conditions allow for a homogeneous velocity field of the particles driven by the fluid.

All simulations analyzed in this paper were performed with 1253 particles and a well-resolved fluid with lattice step $< 0.03d$. The friction coefficient μ_s is set to 0.4 between the particles and to 0 with the top wall. Gravity is set to zero. The bottom wall is made rough by sticking a layer of particles to the bottom of the box. The fluid viscosity η_f is varied in the range $[\eta_w, 2500\eta_w]$, with water viscosity η_w , shear rate $\dot{\gamma}$ in the range $[0.28, 5.6] \text{ s}^{-1}$, confining pressure σ_s in the range $[20, 120] \text{ Pa}$, and relative density r in the range $[0.5, 3]$. The data presented below are average values in the steady state with their error bars representing the standard deviation of fluctuations. The control volume contains the whole volume below the top mobile wall excluding five particle layers adjacent to the walls. Indeed, the velocity profiles are nearly linear except in the five layers close to the walls. Video samples of the simulations can be found in Ref. [11].

III. SCALING WITH MODIFIED INERTIAL NUMBER

Figure 2 displays μ and Φ as a function of both I and I_v . We see that while I and I_v cover a wide range, none of them scales the data points over the whole range. The observed partial correlations of the data reflect either the variation of η_f alone or only that of $\dot{\gamma}$ and σ_s . An important effect that may influence the scaling is the presence of shear-induced lift forces [12]. This leads to a weak stress gradient across the sample so that the vertical pressure acting on the solid phase is different

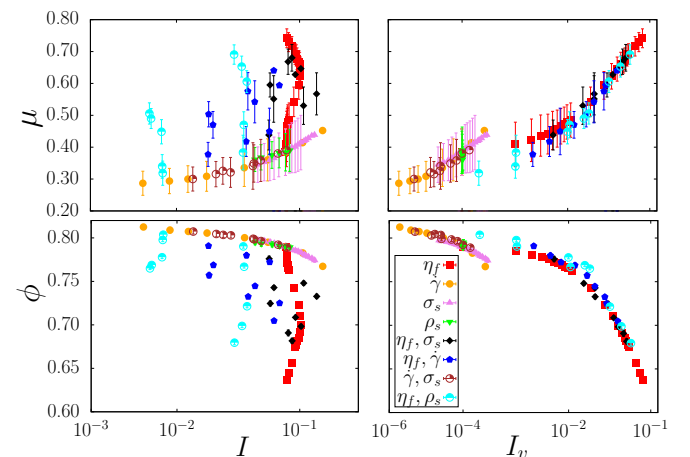


FIG. 2. Bulk friction coefficient μ and packing fraction Φ as a function of control parameters I and I_v . Each symbol and its color refers to a group of simulations in which only one or two parameters were varied as indicated in the inset to the lower right figure.

from the applied stress σ_s . This can be analyzed by calculating the stress tensor from the forces between the particles. In the data presented in Fig. 2 and in all figures presented below, this effect is accounted for by replacing σ_s by $\sigma_n = \sigma_s + \sigma_L$, where σ_L is the average vertical stress induced by lift forces. Up to this weak correction of the confining stress, the query is whether a single dimensionless parameter, possibly combining I and I_v , can be found to scale the data for all system parameters.

In order to recombine all parameters in a single meaningful variable, we consider the characteristic stresses acting on particles. Note that from each characteristic stress Σ , a characteristic time $T = d(\rho_s/\Sigma)^{1/2}$ can be defined. The system involves three stresses of different origins:

- (1) the static stress σ_n ,
- (2) the viscous stress $\sigma_v \sim \eta_f \dot{\gamma}$,
- (3) the inertial stress $\sigma_i \sim \rho_s (d\dot{\gamma})^2$.

The corresponding characteristic times are $t_s = d(\rho_s/\sigma_n)^{1/2}$, $t_v = d(\rho_s/\eta_f \dot{\gamma})^{1/2}$, and $t_i = \dot{\gamma}^{-1}$, respectively. We also have the Stokes time $t_{St} = \eta_f/\sigma_n$, which is simply a function of the three other times: $t_{St} = t_i(t_s/t_v)^2$. From these three time scales, two independent dimensionless numbers can be built: $I = t_s/t_i = (\sigma_i/\sigma_n)^2$ and $J = t_s/t_v = (\sigma_v/\sigma_n)^{1/2} = (\eta_f \dot{\gamma}/\sigma_n)^{1/2}$. The latter is simply the square root of I_v . The ratio $St = (t_v/t_i)^2 = \sigma_i/\sigma_v = I^2/J^2 = \rho_s d^2 \dot{\gamma}/\eta_f$ is the Stokes number.

The total shear stress τ in steady flow is the sum of static, inertial, and viscous stresses, and the visco-inertial regime is, by definition, governed by the sum of viscous and inertial stresses in comparison to the static stress. Hence, the natural combination characterizing the visco-inertial regime is $(\alpha_i \sigma_i + \alpha_v \sigma_v)/\sigma_n = \alpha_i I^2 + \alpha_v J^2 = I^2(\alpha_i + \alpha_v/St)$, where α_i and α_v are constant parameters to be determined. Taking the square root of this ratio, we get a *modified* inertial number

$$I_m = I \left(\alpha_i + \frac{\alpha_v}{St} \right)^{1/2}, \quad (1)$$

which can be called the visco-inertial number. If this number is equivalent to the inertial number I when $St \rightarrow \infty$, we get $\alpha_i = 1$. Hence, the parameter space of the visco-inertial regime can be reduced only if the functions $\Phi(I_m)$ and $\mu(I_m)$ are uniquely defined for a constant value of α_v that reflects the details of interactions at the particle level.

Figure 3 shows μ and Φ as a function of I_m for $\alpha_v = 2.0$, which allows for a remarkable collapse of all our simulation data up to a weak statistical error. Not only do all system parameters affect the rheology only through I_m , but we also observe that, consistent with the laminar nature of flow, the data points for different values of the relative density r fall also on the same curve. The parameter r was absent from the simulations of Trulsson *et al.*, and this observation provides strong support for a unified scaling of immersed and dry granular flows.

The functional forms that excellently fit the two plots are

$$\mu(I_m) = \mu_c + \frac{\delta\mu}{1 + b/I_m}, \quad (2)$$

$$\Phi(I_m) = \frac{\Phi_c}{1 + aI_m}, \quad (3)$$

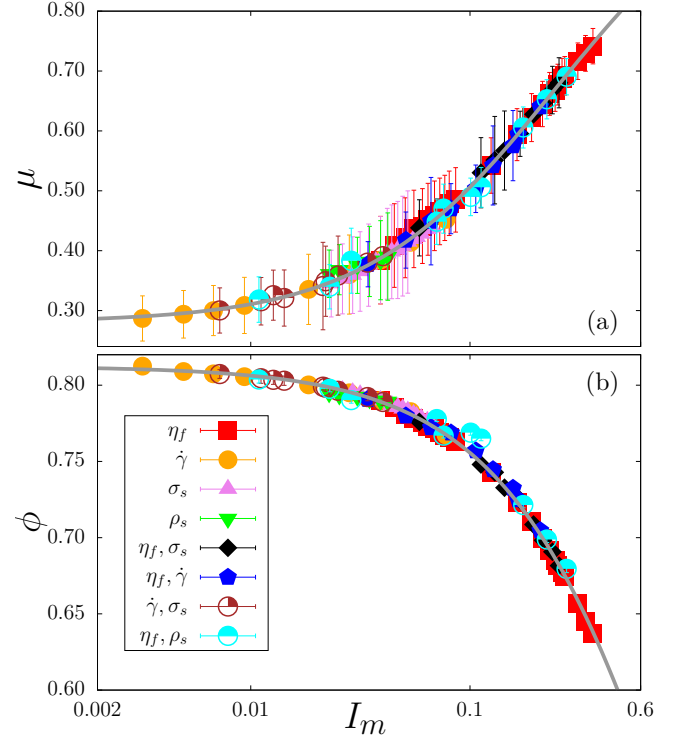


FIG. 3. Bulk friction coefficient μ (a) and packing fraction Φ (b) as a function of the visco-inertial number I_m defined by Eq. (1) with $\alpha_v = 2.0$. The symbols and their colors represent the same groups of simulations as in Fig. 2. The solid lines are the functional forms (2) and (3). The error bars represent the standard deviation of the data.

where $\mu_c = 0.280 \pm 0.002$ is the quasistatic bulk friction coefficient (in contrast to μ_0 , which is a function of I), $\Phi_c = 0.8123 \pm 0.0003$ is the steady-state packing fraction (in contrast to Φ_0 which is a function of I), $b = 0.246 \pm 0.008$, $\delta\mu = 0.783 \pm 0.014$, and $a = 0.750 \pm 0.003$. Note that the scaling of μ and Φ with I_m is strictly the same as in dry granular flows. This is a consequence of the definition of I_m and the choice of $\alpha_i = 1$.

IV. EFFECTIVE VISCOSITIES

In the dual description of the flow, we can express effective viscosities as a function of Φ using the relations (2) and (3). In the presence of particle-inertial forces in addition to viscous forces, σ_t and σ_n at given Φ should scale with $\sigma_i + \alpha_v \sigma_v$:

$$\sigma_t = c_t(\sigma_i + \alpha_v \sigma_v) \equiv c_t \sigma_n I_m^2, \quad (4)$$

$$\sigma_n = c_n(\sigma_i + \alpha_v \sigma_v) \equiv c_n \sigma_n I_m^2, \quad (5)$$

where c_t and c_n play the roles of dimensionless effective viscosities in the visco-inertial regime. We see that they are given by $c_n = 1/I_m^2$ and $c_t = \mu/I_m^2$, leading to the following analytic expressions readily deduced from (2) and (3):

$$c_n = a^2 \left(\frac{\Phi}{\Phi_c - \Phi} \right)^2, \quad (6)$$

$$c_t = a^2 \left(\frac{\Phi}{\Phi_c - \Phi} \right)^2 \left\{ \mu_c + \frac{\delta\mu}{1 + ab \frac{\Phi}{\Phi_c - \Phi}} \right\}. \quad (7)$$

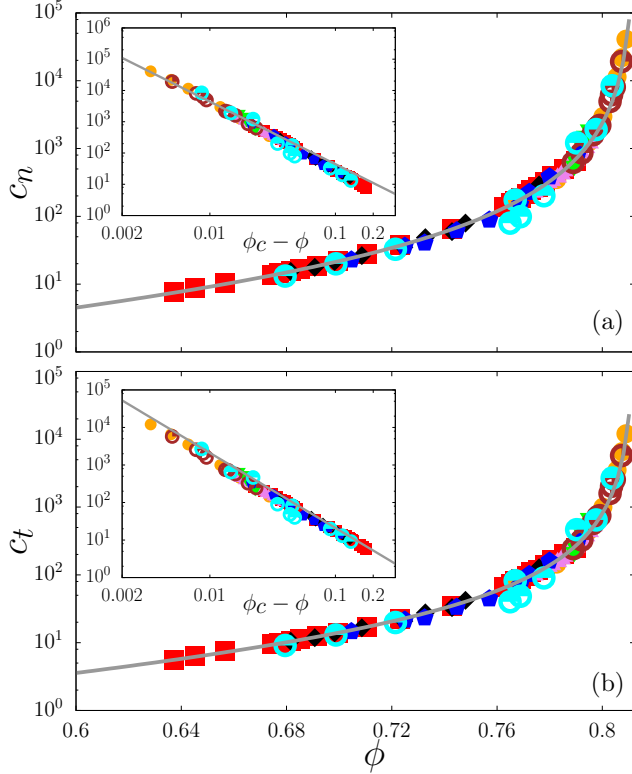


FIG. 4. Effective normal viscosity c_n (a) and shear viscosity c_t (b) as a function of packing fraction from the simulation data. The symbols and their colors represent the same groups of simulations as in Fig. 2. The fits are the analytical expressions (6) and (7).

Figure 4 shows that these expressions are in excellent agreement with our data, and both viscosities diverge as $(\Phi_c - \Phi)^{-2}$ for $\Phi \rightarrow \Phi_c$, consistent with results of Boyer *et al.* and Trulsson *et al.* [4,6]. Note that in the viscous limit where $St \rightarrow 0$ ($I_m \rightarrow (\alpha_v I_v)^{1/2}$), we have $c_n \rightarrow \eta_n / (\alpha_v \eta_f)$ and $c_t \rightarrow \eta_t / (\alpha_v \eta_f)$. Hence, c_n and c_t can be viewed as a generalization of η_n and η_t to the visco-inertial regime. Equivalently, $1/c_n = I_m^2$ represents the generalized fluidity of the suspension [13].

V. EFFECT OF FLUID ON GRANULAR TEXTURE

This remarkable scaling of macroscopic variables with I_m reflects the joint effects of particle inertia and fluid viscous forces on the particles. However, it is crucial for a better understanding of the flow to see to what extent the underlying texture properties are controlled by I_m . In particular, we consider here the fabric and force anisotropies and their relationship with the visco-inertial number. The fabric anisotropy a_c of the contact network describes the excess of the number of contacts oriented along the principal strain-rate direction θ_ϵ and their lack along the perpendicular direction $\theta_\epsilon + \pi/2$. The normal force anisotropy a_n reflects the larger value of the mean normal force at contacts oriented along the principal stress direction θ_σ compared to those in the perpendicular direction $\theta_\sigma + \pi/2$. The tangential force anisotropy a_t quantifies the stronger mobilization of friction forces at contacts oriented along $\theta_\epsilon \pm \pi/4$ compared to those

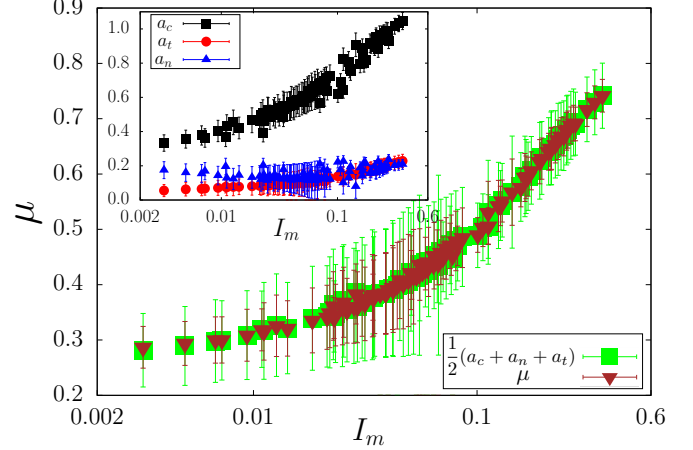


FIG. 5. Effective friction coefficient as a function of the visco-inertial number I_m calculated both from the raw data and from Eq. (8). The inset displays the evolution of the anisotropies as a function of I_m .

in the principal direction θ_ϵ ; see Appendix B for more details on the definition of these variables and their connection with the stress tensor.

By assuming $\theta_\epsilon = \theta_\sigma$, an additive partition of the stress tensor leads to [14–17]

$$\mu(I_m) \simeq \frac{1}{2} \{a_c(I_m) + a_n(I_m) + a_t(I_m)\}. \quad (8)$$

This is an outstanding relationship as it reveals the origins of shear strength in granular flows, herein expressed as a function of I_m . Figure 5 shows μ as a function of I_m both directly obtained from the simulation data and calculated using Eq. (8). We see that the latter holds for all values of I_m . The inset shows the three anisotropies as a function of I_m . The fabric anisotropy a_c increases monotonically with I_m whereas the tangential force anisotropy a_t increases to a lesser extent and a_n declines.

Since μ is the half-sum of the three anisotropies and the normal and tangential force anisotropies add up to a nearly constant value, the main contribution to the increase of μ arises from the strong increase of a_c , as observed also in dry granular flows [16]. Correlatively, the divergence of the shear and normal viscosities as $I_m \rightarrow 0$ is accompanied by a decrease of fabric anisotropy. This is consistent with the fact that the packing fraction increases as the static limit is approached, and the anisotropy tends to decrease as packing fraction increases [18]. More importantly, Fig. 5 shows that the visco-inertial number provides a unique control parameter not only for the macroscopic flow parameters but also for the anisotropy parameters.

The scaling of anisotropy parameters with the visco-inertial number is not an evident property. It reflects the fact that the fluid affects the behavior by allowing for larger contact network anisotropy and stronger force chains. Not all texture parameters are expected to follow this scaling. For example, the coordination number Z does not follow this scaling, as shown in Fig. 6. This fact does not, however, affect the shear strength μ since the coordination number Z does not enter the expression (8). We may attribute this absence of scaling for Z by the effect of lubrication forces between near-neighboring

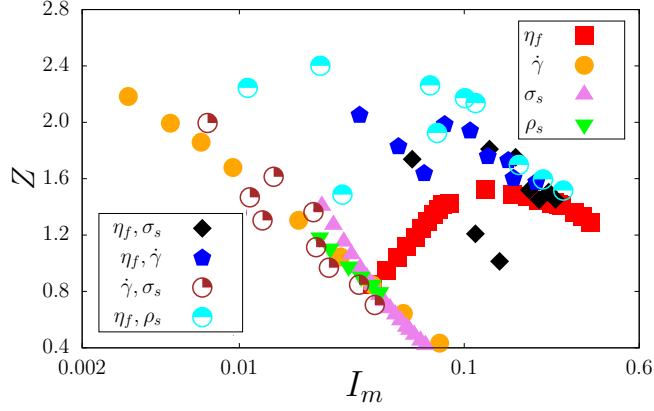


FIG. 6. The coordination number as a function of I_m in all simulations. The symbols and their colors represent the same groups of simulations as in Fig. 2.

particles. These forces depend on the shear rate and viscosity but not on the confining pressure. For the shear stress, the important parameter is not the number of contacts but rather how their orientations are distributed in different directions.

VI. CONCLUSIONS

In summary, our extensive simulations of non-Brownian particles in a sheared suspending fluid provide strong evidence that the parameter space can be reduced to a single *visco-inertial number*, which can also be interpreted as a generalized *fluidity* parameter of the suspension tending to the inverse of effective viscosity in the viscous limit. The robustness of the visco-inertial number was shown for frictional and viscous descriptions of the flow as well as for the granular microstructure by varying several system parameters, including relative fluid-grain density, in a broad range of values. The rheology is mainly governed by the contact network anisotropy reflecting the joint effects of viscous and inertial stresses. Our results obtained by means of subparticle computational fluid dynamics simulations considerably extend the scope of a unique framework introduced by Trulsson *et al.* [6] to a more general parameter space and to the descriptors of microstructural anisotropy. It opens the way also to detailed analysis of local evolutions of pore pressures and contact networks. Despite computational effort, the extension of this investigation to 3D and turbulent flows is desirable.

ACKNOWLEDGMENT

The authors would like to thank the IRSN (French authority of nuclear safety) for financial support.

APPENDIX A: NUMERICAL METHOD

In LBM, the fluid is described by the time-dependent distribution function $f(\mathbf{r}, \mathbf{v}, t)$ of particle positions \mathbf{r} and velocities \mathbf{v} . The spatiotemporal evolution of f is governed

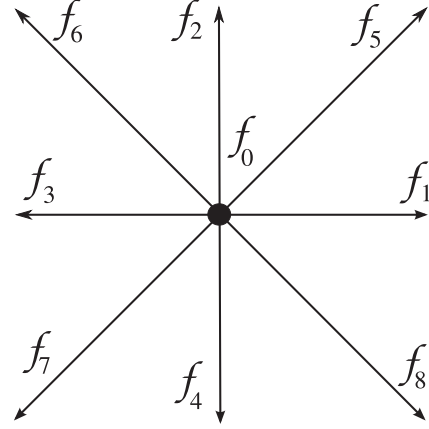


FIG. 7. D2Q9 scheme.

by the Boltzmann equation:

$$\left(\frac{\partial}{\partial t} + \mathbf{v} \cdot \frac{\partial}{\partial \mathbf{r}} + \frac{\mathbf{F}(\mathbf{r})}{m} \cdot \frac{\partial}{\partial \mathbf{v}} \right) f(\mathbf{r}, \mathbf{v}, t) = \Omega_{\text{coll}}, \quad (\text{A1})$$

where m is the particle mass, $\mathbf{F}(\mathbf{r})$ summarizes external forces, and Ω_{coll} represents the collision operator describing the dynamics of collisions between fluid particles. The simplest collision model is the BGK (Bhatnagar-Gross-Krook) operator [19]:

$$\Omega_{\text{BGK}} = -\frac{1}{\tau}(f - f^0) \quad (\text{A2})$$

where τ is the relaxation time and f^0 is the Maxwell-Boltzmann distribution. It is shown that the Boltzmann equation with the BGK collision operator yields to the Navier-Stokes equations [20]. The central idea of LBM [21–23] is to discretize the velocity vector space in a finite number of directions. We used the so-called D2Q9 (two dimensions with nine velocity directions), as shown in Fig. 7. A distinct distribution function f_i is associated to each velocity direction \mathbf{e}_i .

The discretized equations along different directions are solved in two steps:

$$\begin{aligned} \text{Collision : } f_i^{\text{out}}(\mathbf{r}, t) &= f_i(\mathbf{r}, t) + \Omega_i, \\ \text{Streaming : } f_i(\mathbf{r} + \Delta t \mathbf{e}_i, t + \Delta t) &= f_i^{\text{out}}(\mathbf{r}, t), \end{aligned} \quad (\text{A3})$$

where Δt is the time step and the $f_i^{\text{out}}(\mathbf{r}, t)$ are the distribution functions after the collision step. The density $\rho(\mathbf{r}, t)$ and fluid velocity $\mathbf{u}(\mathbf{r}, t)$ are obtained as follows:

$$\begin{aligned} \rho(\mathbf{r}, t) &= \sum_i f_i(\mathbf{r}, t), \\ \rho(\mathbf{r}, t) \mathbf{u}(\mathbf{r}, t) &= \sum_i f_i(\mathbf{r}, t) \mathbf{e}_i. \end{aligned} \quad (\text{A4})$$

The BGK operator is simple but leads to fluctuating velocity fields. In our simulations, we used instead a multirelaxation time (MRT) collision approach [24,25]. It consists in associating nine moments to every fluid node, corresponding to the nine distribution functions, through a matrix \mathbf{M} such that

$$\mathbf{m} = \mathbf{M} \mathbf{f} \quad (\text{A5})$$

where $\mathbf{m} = (m_0, m_1, \dots, m_8)^T$ is the moment vector, $\mathbf{f} = (f_0, f_1, \dots, f_8)^T$ and \mathbf{M} is given by

$$\mathbf{M} = \begin{pmatrix} 1 & 1 & 1 & 1 & 1 & 1 & 1 & 1 & 1 \\ -4 & -1 & 2 & -1 & 2 & -1 & 2 & -1 & 2 \\ 4 & -2 & 1 & -2 & 1 & -2 & 1 & -2 & 1 \\ 0 & 1 & 1 & 0 & -1 & -1 & -1 & 0 & 1 \\ 0 & -2 & 1 & 0 & -1 & 2 & -1 & 0 & 1 \\ 0 & 0 & 1 & 1 & 1 & 0 & -1 & -1 & -1 \\ 0 & 0 & 1 & -2 & 1 & 0 & -1 & 2 & -1 \\ 0 & 1 & 0 & -1 & 0 & 1 & 0 & -1 & 0 \\ 0 & 0 & 1 & 0 & -1 & 0 & 1 & 0 & -1 \end{pmatrix}.$$

Hence, the collision step is applied in the moment space, each moment m_i being relaxed to its equilibrium state m_i^{eq} with a relaxation time s_i . The moments corresponding to the density $\rho(\mathbf{r}, t)$ and the flux $\mathbf{j}(\mathbf{r}, t) = \rho(\mathbf{r}, t)\mathbf{u}(\mathbf{r}, t)$ are conserved. The moment vector \mathbf{m}^{out} resulting from collision can be written as follows:

$$\mathbf{m}^{\text{out}} = \mathbf{m} - \mathbf{S}(\mathbf{m} - \mathbf{m}^{\text{eq}}), \quad (\text{A6})$$

where $\mathbf{S} = \text{diag}(0, s_1, s_2, 0, s_4, 0, s_6, s_7, s_8)$ is a diagonal 9×9 matrix. All relaxation times are proportional to τ^{-1} [26]. The equilibrium moment vector \mathbf{m}^{eq} is given by

$$\mathbf{m}^{\text{eq}} = \begin{bmatrix} \rho \\ -2\rho + 3(j_x^2 + j_y^2)/\rho \\ \rho - 3(j_x^2 + j_y^2)/\rho \\ j_x \\ -j_x \\ j_y \\ -j_y \\ (j_x^2 - j_y^2)/\rho \\ j_x j_y / \rho \end{bmatrix}. \quad (\text{A7})$$

The distribution functions $f_i^{\text{out}}(\mathbf{r}, t)$ resulting from the collision step are given by $\mathbf{f}^{\text{out}} = \mathbf{M}^{-1}\mathbf{m}^{\text{out}}$. Finally, the streaming step is applied in the velocity space.

The no-slip boundary conditions are implemented through the bounce-back rule which consists of reflecting back the incoming distribution functions at a boundary node to their original fluid nodes in the opposite direction $iopp$ ($\mathbf{e}_i + \mathbf{e}_{iopp} = \mathbf{0}$):

$$f_{iopp}^{\text{in}}(\mathbf{r}, t + \Delta t \mathbf{e}_i) = f_i^{\text{out}}(\mathbf{r}, t). \quad (\text{A8})$$

The equations of motion of the particles are solved by means of the MD method [27,28]. The normal force \mathbf{F}_N between a pair (i, j) of touching particles is governed by a viscoelastic law:

$$\mathbf{F}_N = \begin{cases} (-k_n \delta_{ij} - \gamma_n \dot{\delta}_{ij}) \mathbf{n}_{ij} & \text{if } \delta_{ij} < 0 \\ \mathbf{0} & \text{otherwise} \end{cases}, \quad (\text{A9})$$

where δ_{ij} is the gap or the overlap, $\dot{\delta}_{ij}$ is its derivative with respect to time, k_n is the stiffness, and γ_n is a viscous damping parameter which controls restitution coefficient. The friction force \mathbf{F}_T obeys the dry Coulomb law:

$$\mathbf{F}_T = -\min\{\gamma_t \|\mathbf{v}_t\|; \mu_s \|\mathbf{F}_N\|\} \mathbf{t}_{ij}, \quad (\text{A10})$$

where \mathbf{v}_t the tangential velocity at contact, γ_t is the tangential viscosity parameter, and μ_s is the friction coefficient.

The particles are meshed on the lattice grid and represented by solid nodes. The interaction between particles and fluid occurs at their interface. The solid nodes are considered as moving boundaries over which the no-slip condition is imposed [29]. On the other hand, the hydrodynamic forces acting on particles are calculated by the momentum exchange method proposed in Ref. [30].

APPENDIX B: FABRIC AND FORCE ANISOTROPIES

In this section, we introduce the fabric and force anisotropies and their relation with the shear stress in 2D. The stress tensor $\boldsymbol{\sigma}$ can be expressed as [17,31]

$$\sigma_{\alpha\beta} = n_c \langle f_\alpha^c \ell_\beta^c \rangle, \quad (\text{B1})$$

where n_c is the number density of interparticle contacts and the averaging runs over all contacts c with contact force f_α^c and branch vector ℓ_β^c joining the centers of contacting particles. The effective friction coefficient in shear is given by $\mu \simeq q/p$, where $p = (\sigma_1 + \sigma_2)/2$ is the mean pressure in the particle phase and $q = (\sigma_1 - \sigma_2)/2$ is the stress deviator, and σ_1 and σ_2 are the principal values on the shear plane.

The average in (B1) can be expressed as an integral equation:

$$\sigma_{\alpha\beta} = n_c \iiint f_\alpha \ell_\beta P_{\ell f} d\mathbf{f} d\boldsymbol{\ell}, \quad (\text{B2})$$

where $P_{\ell f}$ is the joint probability density of forces and branch vectors $\boldsymbol{\ell} = \ell \mathbf{n}$. Neglecting the weak force-fabric correlations, we may express P as a product $P_{\ell f} = P_\ell(\ell) P_n(\mathbf{n}) P_f(\mathbf{f})$. Integrating over \mathbf{f} and ℓ we get

$$\sigma_{\alpha\beta} \simeq n_c \ell_0 \int_\Omega \langle f_\alpha \rangle(\mathbf{n}) n_\beta P_n(\mathbf{n}) d\mathbf{n}, \quad (\text{B3})$$

where Ω is the angular domain of integration and $\langle \mathbf{f} \rangle(\mathbf{n})$ is the average force as a function of \mathbf{n} and $\ell_0 = \langle \ell \rangle$.

The contact force can be decomposed into its normal and tangential components $\langle f_n \rangle(\mathbf{n})$ and $\langle f_t \rangle(\mathbf{n})$, and \mathbf{n} is parametrized by its orientation θ . The three functions $P(\theta)$, $\langle f_n \rangle(\theta)$, and $\langle f_t \rangle(\theta)$ are π periodic, and they can be well approximated by their lowest-order Fourier expansions [14,16,32,33]:

$$\begin{aligned} P(\theta) &\simeq 1/\pi [1 + a_c \cos 2(\theta - \theta_c)], \\ \langle f_n \rangle(\theta) &\simeq f_0 [1 + a_n \cos 2(\theta - \theta_n)], \\ \langle f_t \rangle(\theta) &\simeq -f_0 a_t \sin(\theta - \theta_t), \end{aligned} \quad (\text{B4})$$

where a_c , a_n , and a_t are anisotropy parameters and $\theta_c \simeq \theta_n \simeq \theta_t$ are the corresponding privileged directions. f_0 is the mean force. All these directions nearly coincide with the major principal stress direction in the steady state. By introducing Eqs. (B4) in the integral (B2) and neglecting the cross products of the anisotropy parameters, one gets the simple relation

$$\mu \simeq \frac{1}{2}(a_c + a_n + a_t). \quad (\text{B5})$$

Figure 5 shows that this relation holds excellently for all values of I_m .

- [1] K. D. Nguyen, S. Guillou, J. Chauchat, and N. Barbry, *Adv. Water Res.* **32**, 1187 (2009).
- [2] F. Legros, *Eng. Geol.* **63**, 301 (2002).
- [3] C. Lareo, P. Fryer, and M. Barigou, *Food Bioprod. Process.* **75**, 73 (1997).
- [4] F. Boyer, E. Guazzelli, and O. Pouliquen, *Phys. Rev. Lett.* **107**, 188301 (2011).
- [5] G. D. R. Midi, *Eur. Phys. J. E* **14**, 341 (2004).
- [6] M. Trulsson, B. Andreotti, and P. Claudin, *Phys. Rev. Lett.* **109**, 118305 (2012).
- [7] S. Courrech du Pont, P. Gondret, B. Perrin, and M. Rabaud, *Phys. Rev. Lett.* **90**, 044301 (2003).
- [8] X. He and L.-S. Luo, *Phys. Rev. E* **56**, 6811 (1997).
- [9] D. Qi, *J. Fluid Mech.* **385**, 41 (1999).
- [10] P. Mutabaruka, J.-Y. Delenne, K. Soga, and F. Radjai, *Phys. Rev. E* **89**, 052203 (2014).
- [11] www.cgp-gateway.org/ref037.
- [12] P. Cherukat, J. McLaughlin, and A. Graham, *Int. J. Multiphase Flow* **20**, 339 (1994).
- [13] L. Bocquet, A. Colin, and A. Ajdari, *Phys. Rev. Lett.* **103**, 036001 (2009).
- [14] L. Rothenburg and R. J. Bathurst, *Geotechnique* **39**, 601 (1989).
- [15] F. Radjai, D. E. Wolf, M. Jean, and J.-J. Moreau, *Phys. Rev. Lett.* **80**, 61 (1998).
- [16] E. Azéma and F. Radjai, *Phys. Rev. Lett.* **112**, 078001 (2014).
- [17] F. Radjai, J.-N. Roux, and A. Daouadji, *J. Eng. Mech.* **143**, 04017002 (2017).
- [18] F. Radjai, J.-Y. Delenne, E. Azéma, and S. Roux, *Granular Matter* **14**, 259 (2012).
- [19] P. L. Bhatnagar, E. P. Gross, and M. Krook, *Phys. Rev.* **94**, 511 (1954).
- [20] C. Bardos, F. Golse, and D. Levermore, *J. Stat. Phys.* **63**, 323 (1991).
- [21] G. R. McNamara and G. Zanetti, *Phys. Rev. Lett.* **61**, 2332 (1988).
- [22] F. J. Higuera and J. Jiménez, *Europhys. Lett.* **9**, 663 (1989).
- [23] Y. H. Qian, D. D’Humières, and P. Lallemand, *Europhys. Lett.* **17**, 479 (1992).
- [24] D. d’Humières, in *Generalized Lattice Boltzmann Equations Rarefied Gas Dynamics: Theory and Simulations*, Progress in Astronautics and Aeronautics, Vol. 159, edited by B. D. Shizgal and D. P. Weaver (Scientific Research, Wuhan, China, 1992), pp. 450–458.
- [25] P. Lallemand and L.-S. Luo, *Phys. Rev. E* **61**, 6546 (2000).
- [26] A. Mussa, P. Asinari, and L.-S. Luo, *J. Comput. Phys.* **228**, 983 (2009).
- [27] S. Luding, in *Physics of Dry Granular Media*, ATO ASI Series E350, edited by H. J. Herrmann, J.-P. Hovi, and S. Luding (Kluwer, Dordrecht, Netherlands, 1998), p. 285.
- [28] P. A. Cundall and O. D. L. Strack, *Géotechnique* **29**, 47 (1979).
- [29] M. Bouzidi, M. Firdaouss, and P. Lallemand, *Phys. Fluids* **13**, 3452 (2001).
- [30] A. J. C. Ladd, *J. Fluid Mech.* **271**, 285 (1994).
- [31] F. Radjai and V. Richefeu, *Philos. Trans. R. Soc., A* **367**, 5123 (2009).
- [32] F. Radjai, M. Jean, J. J. Moreau, and S. Roux, *Phys. Rev. Lett.* **77**, 274 (1996).
- [33] C. Voivret, F. Radjai, J.-Y. Delenne, and M. S. El Youssoufi, *Phys. Rev. Lett.* **102**, 178001 (2009).